ENVIRONMENTAL STUDIES

The reduced net carbon uptake over Northern Hemisphere land causes the close-to-normal CO_2 growth rate in 2021 La Niña

Junjie Liu[1,2]*, David Baker[3], Sourish Basu[4,5], Kevin Bowman[1], Brendan Byrne[1], Frederic Chevallier[6], Wei He[7], Fei Jiang[7], Matthew S. Johnson[8], Terence L. Kubar[9,1], Xing Li[10], Zhiqiang Liu[11], Scot M. Miller[12], Sajeev Philip[13], Jingfeng Xiao[14], Jeongmin Yun[1], Ning Zeng[5,15]

Copyright © 2024 The Authors, some rights reserved; exclusive licensee American Association for the Advancement of Science. No claim to original U.S. Government Works. Distributed under a Creative Commons Attribution NonCommercial License 4.0 (CC BY-NC).

La Niña climate anomalies have historically been associated with substantial reductions in the atmospheric CO_2 growth rate. However, the 2021 La Niña exhibited a unique near-neutral impact on the CO_2 growth rate. In this study, we investigate the underlying mechanisms by using an ensemble of net CO_2 fluxes constrained by CO_2 observations from the Orbiting Carbon Observatory-2 in conjunction with estimates of gross primary production and fire carbon emissions. Our analysis reveals that the close-to-normal atmospheric CO_2 growth rate in 2021 was the result of the compensation between increased net carbon uptake over the tropics and reduced net carbon uptake over the Northern Hemisphere mid-latitudes. Specifically, we identify that the extreme drought and warm anomalies in Europe and Asia reduced the net carbon uptake and offset 72% of the increased net carbon uptake over the tropics in 2021. This study contributes to our broader understanding of how regional processes can shape the trajectory of atmospheric CO_2 concentration under climate change.

INTRODUCTION

Anthropogenic emissions from fossil fuel burning, cement production, and land use practices are primary drivers for the atmospheric CO_2 increase. However, not all anthropogenic emissions remain in the atmosphere. Land and ocean have absorbed a stable proportion of the anthropogenic emissions so far, maintaining a roughly 44% airborne fraction (AF) (*1*), defined as the ratio between the annual increase in atmospheric CO_2 and the anthropogenic emissions (Fig. 1). The AF has large year-to-year variations, ranging from as low as approximately 20% to as high as 78% (Fig. 1). This variation is mainly driven by the response of tropical land carbon fluxes to climate anomalies caused by the El Niño Southern Oscillation (ENSO) cycle (*2*–*4*). During El Niños, tropical continents are generally warmer and drier, leading to a decrease in carbon uptake from the atmosphere. This, in turn, results in a higher atmospheric CO_2 growth rate and an average of 16% more carbon remaining in the atmosphere (i.e., 60% AF) than the average. Conversely, La Niña events have the opposite effect, causing an average of 9% lower AF compared to the overall average (Fig. 1). Therefore, the extent to which land absorbs carbon from the atmosphere and sustains a larger carbon sink in future La Niña events has consequential implications for climate change and the effectiveness of carbon-climate policies aimed at achieving Paris climate goals.

In 2021, despite being in the middle of the longest La Niña event of this century (28 months; fig. S1), the atmospheric CO_2 growth rate (table S2) was unexpectedly close to historical average, instead of being lower as expected from the historical record (Fig. 1). Since the inception of the modern CO_2 records in 1959, the atmospheric CO_2 growth rate has, on average, been about 0.3 parts per million (ppm) lower than the climatological mean during La Niña events after removing the secular trend (Fig. 1). For example, in 2011, the second longest La Niña event of this century, the atmospheric CO_2 growth rate anomaly was notably negative at −0.5 ppm and the AF at 32%, owing to the anomalous large carbon uptake over Southern Hemisphere (SH) semiarid vegetation (*5*). Intriguingly, the atmospheric CO_2 growth rate anomaly in 2021 was a mere 0.01 ppm, and the AF was 46%, even higher than the average AF. This unique occurrence contrasts sharply with the historical pattern where positive CO_2 growth rate anomalies during La Niña events were extremely rare, with notably anomalies of 0.05 ppm in 1975 and 0.19 ppm in 1985.

Understanding the underlying factors contributing to the near-neutral impact of 2021 La Niña can provide valuable insights into the potential response of the carbon cycle to similar La Niña events and anticipated trajectories of atmospheric CO_2 concentration in the future. El Niño events, known for their substantial influence on both precipitation and tropical carbon cycle, have garnered substantial interest within the scientific community (*6*–*11*). Conversely, research on La Niña events are relatively scarce (*5*). Unlike in 1975 and 1985, in 2021, there were unprecedented CO_2 observations from satellites. Previous studies have shown that the satellite observations from the Orbiting Carbon Observatory-2 (OCO-2) effectively

[1]Jet Propulsion Laboratory, California Institute of Technology, Pasadena, CA 91109, USA. [2]Division of Geological and Planetary Sciences, California Institute of Technology, Pasadena, CA, USA. [3]Cooperative Institute for Research in the Atmosphere, Colorado State University, Fort Collins, CO, USA. [4]Global Modeling and Assimilation Office, NASA Goddard Space Flight Center, Greenbelt, MD, USA. [5]Earth System Science Interdisciplinary Center, College Park, MD 20740, USA. [6]Laboratoire des Sciences du Climat et de L'Environnement, LSCE/IPSL, CEA-CNRS-UVSQ, Université Paris-Saclay, 91191 Gif-sur-Yvette, France. [7]Nanjing University, Nanjing, China. [8]Earth Science Division, NASA Ames Research Center, Moffett Field, CA 94035, USA. [9]Joint Institute for Regional Earth System Science and Engineering, University of California, Los Angeles, Los Angeles, CA 90095, USA. [10]Research Institute of Agriculture and Life Sciences, Seoul National University, Seoul, Republic of Korea. [11]Laboratory of Numerical Modeling for Atmospheric Sciences and Geophysical Fluid Dynamics, Institute of Atmospheric Physics, Chinese Academy of Sciences, Beijing, China. [12]Department of Environmental Health and Engineering, Johns Hopkins University, Baltimore, MD 21218, USA. [13]Centre for Atmospheric Sciences, Indian Institute of Technology Delhi, New Delhi, India. [14]Earth Systems Research Center, Institute for the Study of Earth, Oceans, and Space, University of New Hampshire, Durham, NH 03824, USA. [15]Department of Atmospheric and Oceanic Science, University of Maryland, College Park, MD 20742, USA.
*Corresponding author. Email: junjie.liu@jpl.nasa.gov

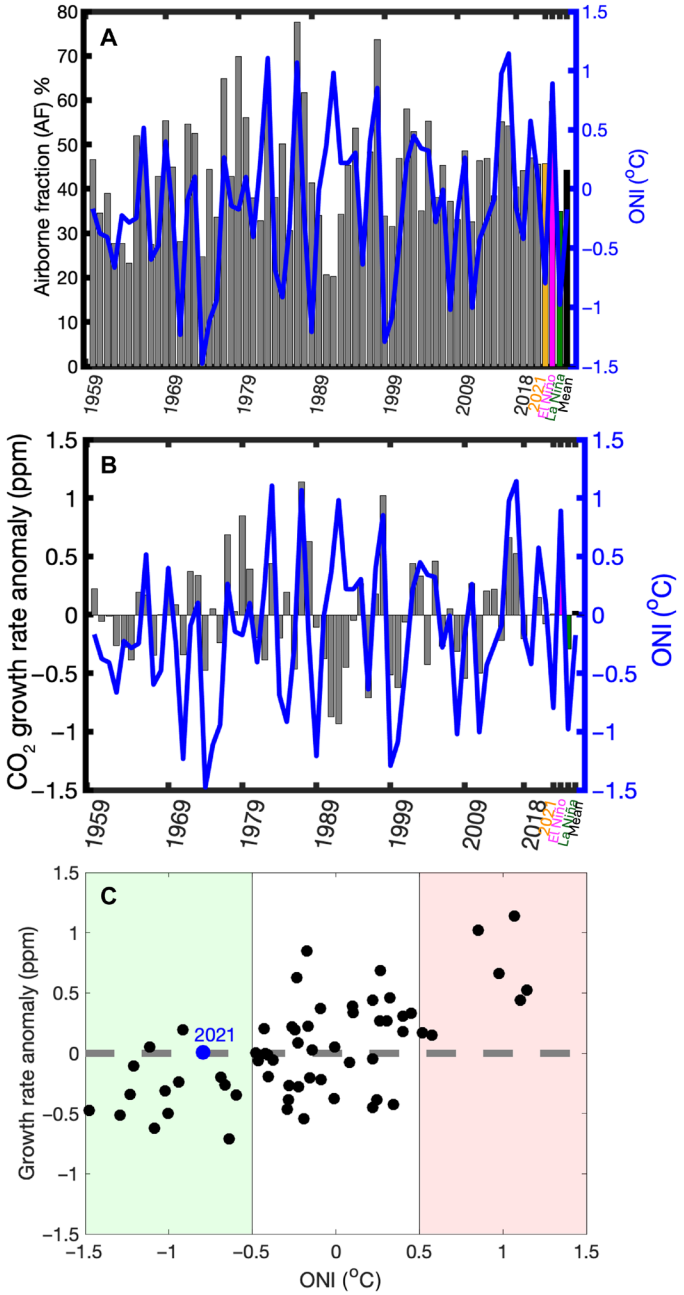

Fig. 1. The atmospheric CO_2 growth rate and airborne fraction (AF) are generally lower during La Niña, while the growth rate in 2021 is close to average despite being in the middle of the longest La Niña in this century. (**A**) AF (bars) and annual mean Oceanic Nino Index (ONI) (Oct-Sep) (unit: °C) between 1959 and 2021 (line). Gray bars, 1959–2020; orange, 2021; green, average AF during La Niña events; magenta, average AF during El Niño events; black, average over 1959–2021. (**B**) CO_2 growth rate anomaly (black) (unit: ppm) and annual mean ONI (Oct-Sep) (unit: °C) between 1959 and 2021. (**C**) Annual ONI index versus CO_2 growth rate anomaly between 1959 and 2021 without 1991 and 1992, when Pinatubo volcano eruption had a dominant impact (*51*). ONI is defined as sea surface temperature (SST) anomalies over Niño 3.4 region (5°N to 5°S, 170°W to 120°W). El Niño years are those with annual mean ONI greater than 0.5°C, and La Niña years are those with annual mean ONI lower than −0.5°C. Note that the annual mean ONI is the mean over Oct-Sep to account for possible lagged response of land climate anomalies to SST anomalies (*37*), while the annual CO_2 growth rate for a given year is the CO_2 difference between the end of December and the start of January of that year based on global marine surface data (https://gml.noaa.gov/ccgg/trends/gl_gr.html).

monitored the response of regional carbon fluxes to climate interannual variations (*9*, *11*–*13*).

In this study, we use an ensemble of CO_2 fluxes estimated from top-down atmospheric inversions assimilating OCO-2 land observations (tables S1 and S2). We also use two satellite-constrained gross primary production (GPP) products and a fire CO_2 emission product from a top-down CO atmospheric inversion (Materials and Methods and table S2) to explore processes that have contributed to the close-to-average atmospheric CO_2 growth rate in 2021 La Niña condition. Specifically, our aim is to assess the land carbon cycle responses at various scales, ranging from hemispheric to continental scales and then down to regions affected by extreme climate anomalies. In addition, we seek to quantify the role played by different vegetation types to examine whether semiarid regions play an outsized role, as observed in the 2011 La Niña. The ensemble net CO_2 fluxes over 2015–2021 were generated with a subset of models that contributed to the v10 Orbiting Carbon Observatory (OCO-2) modeling intercomparison project (MIP) by Byrne *et al.* (*14*) and one additional model, GCASv2, which has been documented in (*15*, *16*). The ensemble top-down inversions capture the sensitivity of flux estimates to transport models, inversion methods, and inversion setups (Materials and Methods) (table S1). The annual net carbon fluxes, calculated as the sum of fossil fuel emissions and natural carbon fluxes over land and ocean, align closely with the annual CO_2 growth rate reported by National Oceanic and Atmospheric Administration (NOAA) (fig. S2) (Materials and Methods).

RESULTS

Responses of hemispheric land carbon fluxes to 2021 La Niña

We calculated annual carbon flux anomalies relative to the mean over 2015–2021 for each year. Over these 7 years, the land net biosphere exchange (NBE) (i.e., including all land-atmosphere CO_2 fluxes except fossil fuel emissions) dominated the year-to-year variations of total natural (land and ocean) carbon fluxes (Fig. 2A), consistent with the long-established understanding that the NBE has stronger interannual variations than the ocean net carbon fluxes (*17*–*20*). In 2021, the NBE anomaly was −0.22 ± 0.15 gigaton carbon (GtC), with negative numbers indicating more net carbon uptake from the atmosphere. Despite 2021 being the strongest La Niña among these 7 years (Fig. 1) (*21*, *22*), the magnitude of net land carbon uptake from the atmosphere was smaller than that in 2017 and 2018 (Fig. 2), which were weak La Niña during part of the year and had −0.74 ± 0.14–GtC and −0.59 ± 0.15–GtC NBE anomalies, respectively.

Breaking down the land into tropics and extra-tropics, we find that the tropical land absorbed 0.79 ± 0.23 GtC more carbon from the atmosphere in 2021, the largest carbon sink during these 7 years, consistent with the notion that a larger carbon sink exists over the tropical land during La Niña years (*3*). Here, the tropical land is defined as the land area within 22°S and 22°N. This increased net carbon uptake in 2021 had a similar magnitude as the anomalous carbon release from the tropical continents during the 2015–2016 El Niño, indicating the strong impact of climate interannual variations due to the ENSO cycle on tropical land carbon fluxes.

However, the extra-tropical land absorbed 0.57 ± 0.30 GtC less carbon from the atmosphere in 2021 (Fig. 2B), offsetting 72% of the increased carbon sink over the tropics. Consequently, land carbon

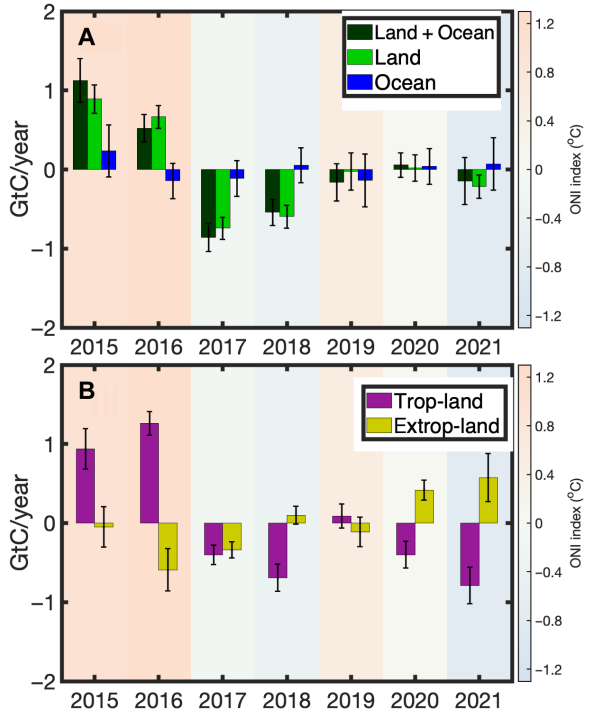

Fig. 2. The reduced net carbon uptake over the extra-tropical land offsets 72% of the increased net carbon uptake over the tropical land, causing the close-to-average atmospheric CO_2 growth rate in 2021, despite being in the middle of the longest La Niña in this century. (**A**) Annual combined land and ocean (dark green), land (light green), and ocean (blue) net carbon flux anomalies estimated by the ensemble top-down atmospheric inversion models (unit: GtC/year). (**B**) The annual NBE anomalies over tropical land (pink) and the extra-tropical land (yellow) (unit: GtC/year) from 2015 to 2021. Positive values indicate less carbon uptake from the atmosphere and vice versa. The sum of the NBE anomalies over the tropical land and the extra-tropical land in (B) is equal to the total land NBE anomaly plotted in (A). The background colors in these two panels are the annual ONI, with warm colors indicating positive SST anomalies while cool light blue indicating negative SST anomalies. Same as in Fig. 1, the annual ONI is defined as mean SST anomalies between October and September in Niño 3.4 region. The uncertainty bars in the figures represent the SDs among the ensemble top-down atmospheric inversion models.

sink only slightly increased in 2021 leading to a nominal CO_2 growth rate. The compensating carbon flux anomalies between the tropics and extra-tropics in 2021 were consistently estimated among all the inversions, and almost all the models indicate that the extra-tropics had the weakest carbon sink in 2021 (fig. S3). Note that the atmospheric CO_2 growth rate anomaly was calculated relative to the mean over 1959–2021 after removing the temporal trend, while the flux anomalies were calculated relative to the mean over 2015–2021, so the total flux anomaly in Fig. 2 does not equal to the growth rate anomaly in Fig. 1.

Previous studies suggest that the CO_2 flux distributions between the tropics and extra-tropics are affected by the errors in model-simulated CO_2 vertical profiles caused by vertical transport errors (*23*, *24*). While the flux anomalies are found to be less sensitive to absolute errors in CO_2 vertical profiles, they could be influenced by the time-varying errors in CO_2 vertical gradient. To assess the robustness of the flux anomaly contrast between the tropics and extra-tropics, we quantified CO_2 vertical gradient errors across three regions—North America, Southeast Asia, and East Asia, where a stable amount of aircraft observations is available—and examined how the CO_2 vertical gradient errors vary by years (Materials and Methods and figs. S4 to S7). We found that the errors in CO_2 vertical gradient are relatively constant in each region over the period that we examined, although the absolute CO_2 vertical gradient errors differing by regions. For example, over Southeast Asia, the CO_2 vertical gradient errors are 0.2 ± 0.3 ppm, 0.2 ± 0.3 ppm, and 0.4 ± 0.2 ppm in 2015, 2016, and 2017, respectively. This suggests that the impact of vertical transport errors on the flux distributions between the tropics and extra-tropics is consistent year to year, supporting the robustness of the flux anomaly contrast between the tropics and extra-tropics. The persistent nature of transport errors was also demonstrated in (*25*).

To further understand the causes for the reduced net carbon uptake over the extra-tropical land, we divided the extra-tropical land into three latitude bands: the Northern Hemisphere (NH) mid-latitudes (23°N to 50°N), the NH high latitudes (50°N to 90°N), and the SH mid-to-high latitudes (23°S to 60°S). We calculated net carbon flux and its component flux anomalies over forest, semiarid region, and grassland/cropland (fig. S8). We find that the net carbon uptake over the NH mid-latitudes reduced by 0.53 ± 0.24 GtC in 2021, dominating the total net carbon uptake reduction over the extra-tropics (0.57 ± 0.30 GtC) (Fig. 3 and fig. S10). Over the SH mid-to-high latitudes, the net carbon uptake increased by 0.09 ± 0.04 GtC in the crop/grassland, and the net carbon uptake decreased by 0.15 ± 0.06 GtC over the NH high latitudes (Fig. 3 and fig. S10), driven by the increased forest fire carbon emissions over Siberia forest (*26*). Because the magnitude of the net carbon flux anomalies over the SH mid-to-high latitudes and the NH high latitudes are much smaller, in the next two sections, we will focus on regional contributions and causes of net carbon flux anomalies over the tropics and the NH mid-latitudes.

Regional contributions and causes of the increased net carbon uptake over the tropics in 2021

Over the tropics, Asia and South America had comparable increases in net carbon uptake, with −0.30 ± 0.13–GtC and −0.28 ± 0.15–GtC NBE anomalies, respectively (Fig. 4). Tropical Africa exhibited a slightly lower increase, with −0.24 ± 0.13–GtC NBE anomaly. Of the −0.30 ± 0.13–GtC NBE anomalies that occurred in tropical Asia, −0.07 ± 0.05 GtC came from the tropical part of Australia, and the NBE anomaly over the rest of Australia was −0.07 ± 0.04 GtC. Thus, the NBE anomaly in Australia was −0.14 ± 0.06 GtC, weaker than the NBE anomalies over any of the tropical continents.

Nearly all NBE anomalies in tropical South America concentrated within the forested area, whereas semiarid regions and grassland/cropland were the majority contributor to the net carbon flux anomalies over the tropical Africa and Asia (Fig. 3). Only 10% of NBE anomalies over tropical Africa originated from forests, while approximately a quarter of the NBE anomalies in tropical Asia were observed in forested regions. In total, the forested regions contributed approximately 46% to the tropical NBE anomalies (Fig. 3), while semiarid and grassland/cropland regions contributed 25 and 30%, respectively.

However, the magnitude of GPP anomalies over the semiarid region and grassland/cropland was approximately three times of that over the forest region (1.37 ± 0.20 GtC versus 0.44 ± 0.24 GtC) in

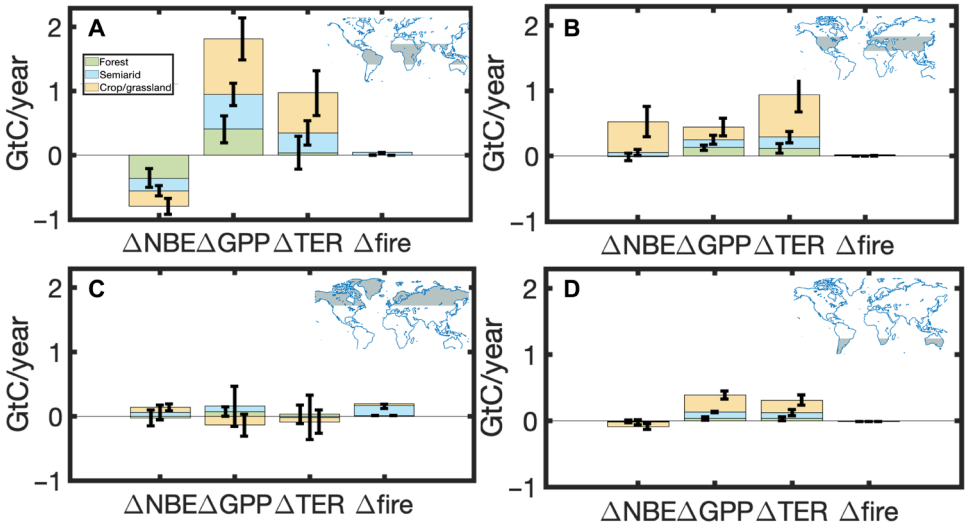

Fig. 3. The decrease in carbon absorption in the mid-latitudes of the NH, mostly from grasslands and croplands, is the main driver for the reduced carbon absorption in extra-tropics, while tropical forests contribute more to increased net carbon uptake than semiarid regions or grasslands. Annual NBE, GPP, TER, and fire emission anomalies in 2021 over forest, semiarid region, and crop land/grassland (the land cover type is based on MODIS IGBP 2020 land cover classification) in the tropics (**A**), the NH mid-latitudes (**B**), the NH high latitudes (**C**), and the SH mid-to-high latitudes (**D**) (unit: GtC/year). The inserted plots on each panel indicate the regions each panel illustrates. A negative ΔNBE corresponds to an increased net carbon uptake from the atmosphere, while a positive ΔGPP indicates increased productivity. Conversely, positive ΔTER and Δfire values suggest more carbon released to the atmosphere.

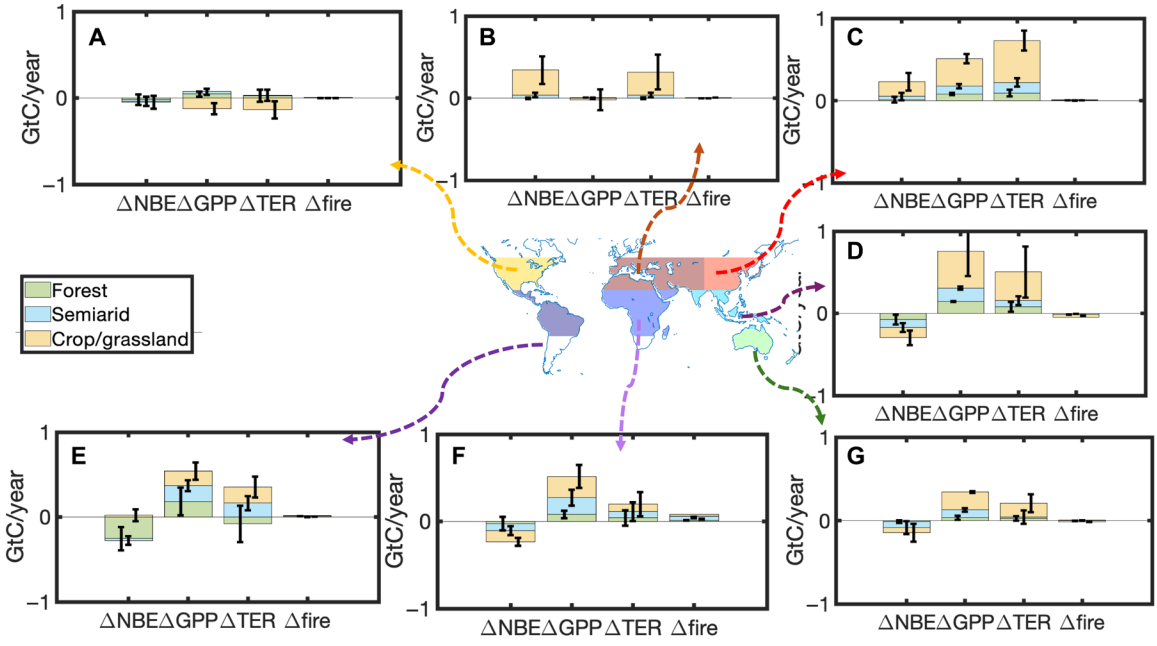

Fig. 4. The overall reduction in net carbon uptake in extra tropical land regions, shown as positive NBE anomalies, is mainly driven by Europe and Asia, while the three tropical continents have comparable NBE anomalies. Annual anomalies of NBE, GPP, TER, and fire in 2021 over mid-latitudes North America (**A**), Eurasia (**B**), East Asia (**C**), tropical Asia (**D**), the mid-latitude Australia (**G**), tropical Africa (**F**), and tropical South America (**E**) (clockwise) in forest, semiarid, and crop land/grassland regions (unit: GtC/year).

the tropics (Fig. 3). Most of the increase in GPP over the semiarid region and grassland/cropland was released into the atmosphere through an increase in total ecosystem respiration (TER) (Figs. 3 and 4) (Materials and Methods), especially over grassland/cropland. This is likely due to the much shorter turnover time of carbon pools in these vegetation types (*27*).

The increase in net carbon uptake across the three tropical regions was primarily driven by increased photosynthesis, corresponding to wetter conditions throughout the year in tropical South America and Asia (figs. S9 to S12). However, tropical Africa experienced lower annual mean precipitation in 2021 compared to the mean over 2015–2021 (figs. S9 and S10). Despite this, the total water

storage anomaly (TWS), indicating total soil water availability, was above average across most of tropical Africa throughout the year (figs. S11 and S13), potentially contributing to the observed increase in GPP over the region. Notably, Madani *et al.* (*28*) similarly noted that higher-than-average groundwater storage offsets the impact of precipitation deficit on GPP over African tropical forest. They found that GPP anomalies exhibit higher correlation with TWS anomalies than with precipitation anomalies over tropical Africa. This is likely due to deeper rooting zone water storage capacity and deeper rooting depth (*29*, *30*).

The most substantial increase in GPP and net carbon uptake in the tropics were observed during the first half of the year and the last 2 months (Fig. 5), coinciding with stronger La Niña and higher precipitation (figs. S1, S11, and S12). Among all these regions, the precipitation increase in tropical South America was the most widespread (figs. S9 and S10). The anomalies in fire carbon emissions amounted to only 0.07 GtC across the entire tropics.

Regional contributions and causes of the deceased net carbon uptake over the NH mid-latitudes in 2021

Different from the tropics, over the NH mid-latitudes, the reduction in net carbon uptake (i.e., positive NBE anomalies) primarily occurred over grassland/cropland in Eurasia and East Asia (Fig. 4). The total net carbon uptake over North America remained close to normal, primarily because of the compensating effect between the increased net carbon uptake in the east and reduced net carbon uptake in the west (fig. S9). In contrast to the tropics, the decrease in net carbon uptake over the NH mid-latitudes was driven by an increase in TER instead of a decrease in GPP (Figs. 3 and 4), particularly over East Asia.

The reduction in net carbon uptake over Eurasia was predominantly observed in regions that experienced extreme climate anomalies in 2021, especially in central Asia (Fig. 6). Averaged over April to June, the temperature anomalies reached up to 3°C above normal, while precipitation decreased by as much as 60 to 80% in central Asia (Fig. 6). These extreme conditions resulted in reduced productivity and increase in ecosystem respiration (Fig. 6). The GPP decreased by over 80% during April to June in a substantial area of central Asia (Fig. 6). On an annual total, the net carbon uptake decreased by 0.39 ± 0.12 GtC over the region from 35°E to 85°E and 30°N to 50°N, accounting for more than half of the total NBE anomalies over the NH mid-latitudes. Approximately half of the NBE anomalies in this region can be attributed to a reduction in GPP (−0.20 ± 0.12 GtC), while the other half results from an increase in TER (0.19 ± 0.17 GtC). The contribution of fire emissions to the reduced net carbon uptake in this region is negligible.

In East Asia, annual GPP increased by 0.52 ± 0.07, but the increase in TER was even larger, with a 0.77 ± 0.15 anomaly. Consequently, net carbon uptake decreased by 0.25 ± 0.12 GtC. The largest reduction in net carbon uptake occurred during spring to early summer (Fig. 7 and fig. S12), predominantly over central and northern China (Fig. 7). This corresponds to high-temperature anomalies and reduced precipitation (*31*) (Fig. 7). During the summer, despite increased productivity in most of East Asia, the net carbon uptake decreased (fig. S12). This implies an increase in ecosystem respiration, possibly

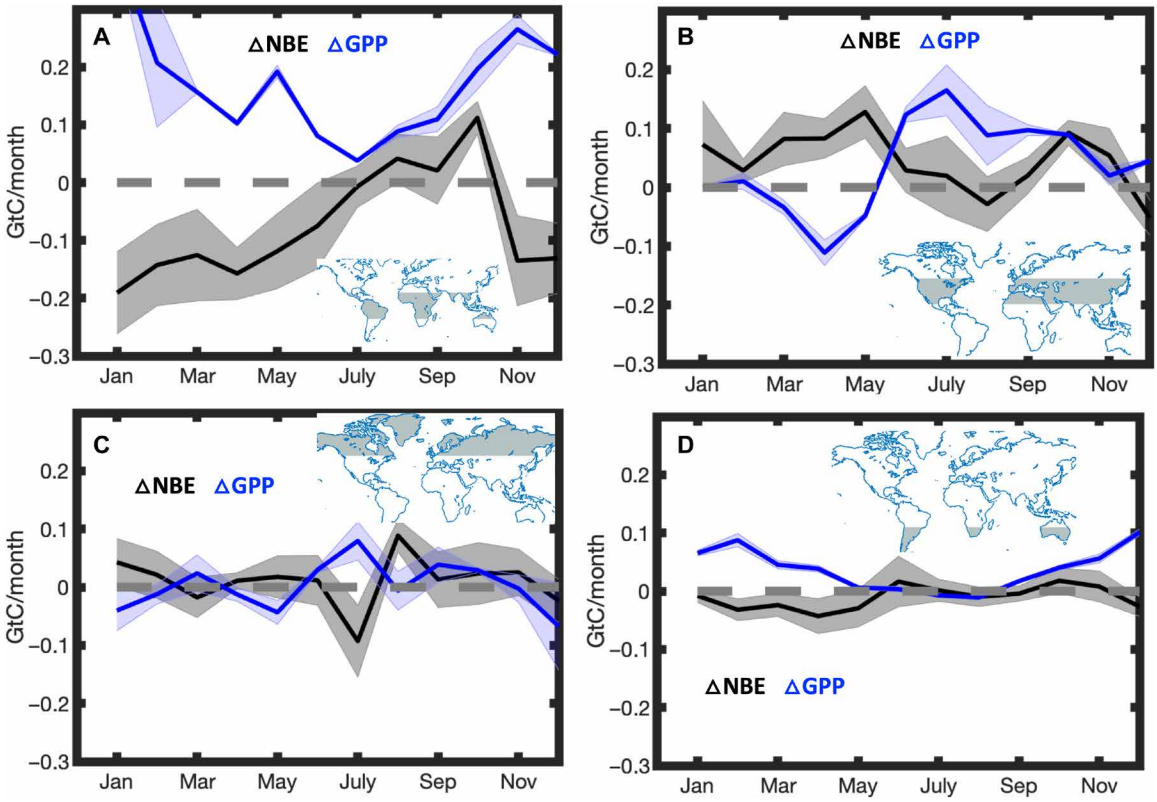

Fig. 5. Independent monthly GPP anomaly and NBE anomaly show anticorrelation in all four latitude bands. (**A** to **D**) Monthly NBE (black) and GPP (blue) anomalies over the tropics (A), NH mid-latitudes (B), NH high latitudes (C), and SH mid-to-high latitudes (D), respectively (unit: GtC/month).

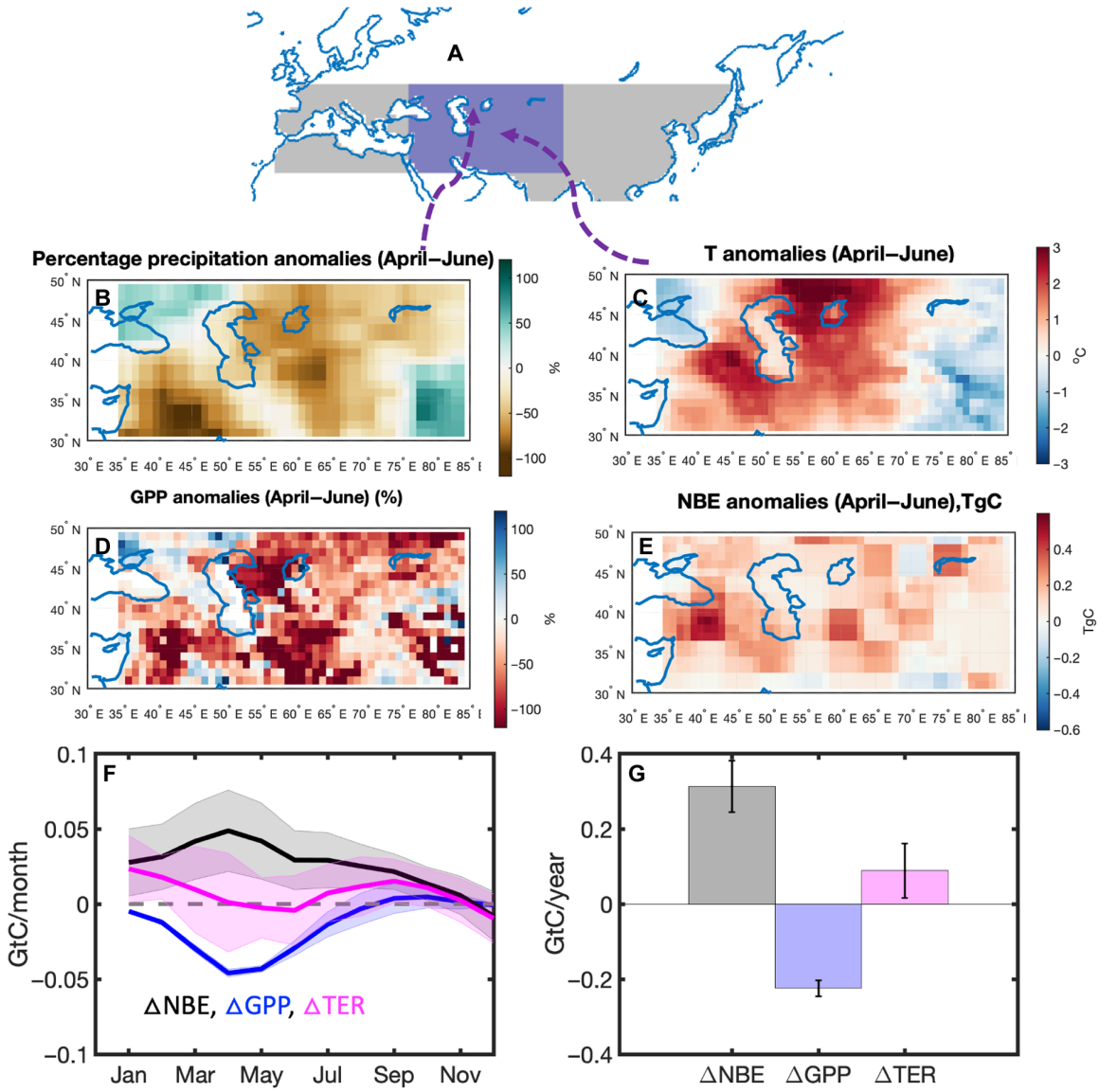

Fig. 6. The extreme drought and warm climate anomalies cause the large reduction of GPP and increase of ecosystem respiration over central Asia, both of which contributes to the reduction of net carbon uptake over the region. (**A**) Regional mask for central Asia (purple) relative to Eurasia regional mask (gray). (**B**) Percentage precipitation anomalies between April and June, 2021 (unit: %) relative to the mean over 2015–2021. (**C**) Temperature anomalies between April and June. (**D**) Percentage change of GPP anomalies between April and June (unit: %). (**E**) NBE anomalies during April to June [unit: tera grams of carbon (TgC)]. (**F**) Monthly anomalies of NBE, GPP, and TER over the region (unit: GtC/month). (**G**) Annual anomalies of NBE, GPP, and TER (unit: GtC/year).

due to much warmer temperatures across the region and drier condition over southern China (Fig. 7 and figs. S9 and S13).

In addition to the ENSO cycle, various teleconnections, including Indian Ocean Dipole, North Atlantic Oscillation, and Arctic Oscillation, have caused carbon flux anomalies over mid-latitudes (*32*–*34*). However, in 2021, these teleconnections were observed to be within normal ranges (fig. S14), suggesting that the mid-latitude carbon flux anomalies in 2021 were not influenced by these teleconnections.

The impact of fossil fuel emission uncertainties on flux anomaly estimation over East Asia

Our results reveal a decrease in net carbon uptake in East Asia for the year 2021 despite increases in GPP. We posit that the higher-than-normal temperatures during spring and later in the year contribute to the elevated terrestrial biosphere respiration, ultimately leading to a reduction in net carbon uptake across the region.

However, it is crucial to acknowledge that this conclusion relies on the accuracy of fossil fuel emission anomalies used in the top-down inversions. We calculate NBE anomalies by subtracting fossil fuel emission anomalies from the total flux anomalies, assuming the accuracy of the former. This assumption is grounded in the observation that the relative uncertainties in fossil fuel emission inventories are smaller compared to natural carbon fluxes (*17*). Nonetheless, it is important to note that the relative uncertainties of fossil fuel emissions can be considerably much larger on regional scales (*35*, *36*), and this uncertainty may be reflected in the NBE estimates.

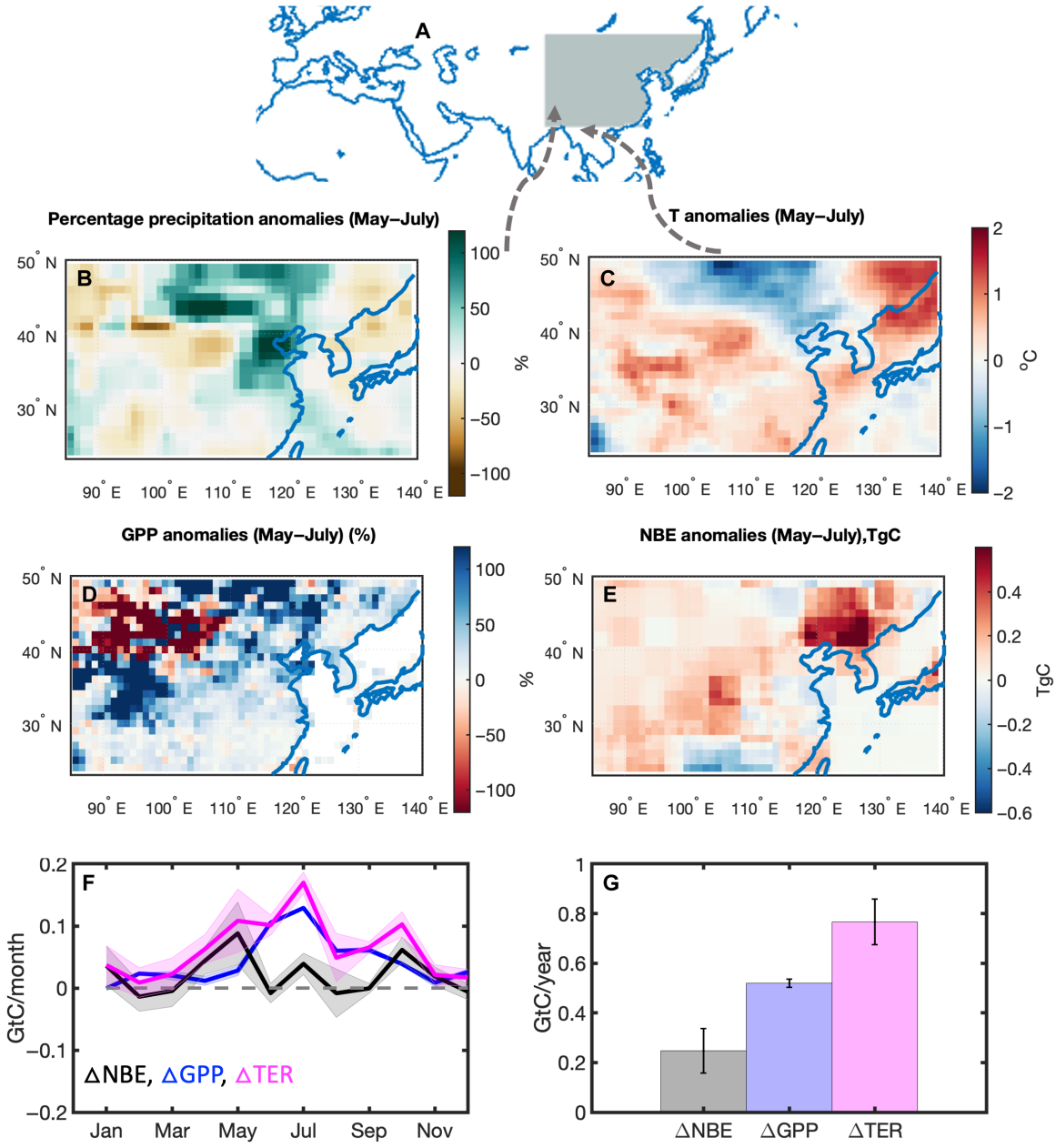

Fig. 7. The warm temperature anomalies caused the increase in ecosystem respiration over East Asia, outpacing the GPP increase. (**A**) Regional mask for East Asia (gray). (**B**) Percentage precipitation anomalies between May and July, 2021 (unit: %) relative to the mean over 2015–2021. (**C**) Temperature anomalies between May and July. (**D**) Percentage change of GPP anomalies between May and July (unit: %). (**E**) NBE anomalies during May to July [unit: tera grams of carbon (TgC)]. (**F**) Monthly anomalies of NBE, GPP, and TER over the region (unit: GtC/month). (**G**) Annual anomalies of NBE, GPP, and TER (unit: GtC/year).

Given East Asia's large magnitude of fossil fuel emissions, totaling 3.5 GtC in 2021 based on the Open-source Data Inventory for Atmospheric CO2 (ODIAC) fossil fuel emission inventory (fig. S15), and the substantial uncertainties in emission trends, NBE estimates for this region may exhibit heightened vulnerability to uncertainties in fossil fuel emissions. To assess the potential impact of uncertainties in fossil fuel emissions on the calculation of NBE anomalies in East Asia, we compared the fossil fuel emissions used in our study with those from the Gridded Fossil fuel Emission Dataset (GridFED), as reported in GCP 2022 (*17*). In our investigation, all eight inversion models used the same fossil fuel emission data from ODIAC (refer to Materials and Methods and table S1). The annual totals for both 2020 and 2021 were derived from near-real-time fossil fuel emission data from Carbon Monitor, and the spatial distribution was based on ODIAC.

Our findings indicate that the fossil fuel emission anomaly in 2021, relative to the mean between 2015 and 2021, is 0.17 GtC for both inventories over East Asia (fig. S15), consistent with each other, albeit with a mean difference of 0.1 GtC. Even at the monthly time scale, the fossil fuel emissions agree on the magnitude of anomalies,

though they differ in their seasonality (fig. S16). Furthermore, the magnitude of monthly fossil fuel emission anomalies is much smaller than that of NBE anomalies (fig. S17). It is noteworthy that NBE anomalies are only responsive to fossil fuel emission anomalies, rather than being influenced by the absolute values of fossil fuel emissions. This is attributed to the removal of annual/monthly mean fluxes during the calculation of annual/monthly flux anomalies.

Assuming a 20% uncertainty in fossil fuel emission anomalies over East Asia, implying a range from 0.13 to 0.21 GtC for fossil emission anomalies, we propagated this uncertainty into the calculation of NBE anomalies. Consequently, the NBE anomalies over East Asia integrated over all vegetation types were determined to be 0.25 ± 0.13 GtC, reaffirming their robustness.

DISCUSSION

Comparisons to the response of terrestrial biosphere carbon cycle to the 2011 La Niña event

Our results reveal a substantial increase in the net carbon sink over tropical land in 2021, marking the largest tropical carbon sink observed between 2015 and 2021. Conversely, the SH NBE anomaly is only -0.08 ± 0.04 GtC. Notably, the tropical forest contributes approximately 50% while the semiarid region contributes 20 to 30% to the overall increased tropical and SH net carbon uptake anomalies. These results stand in stark contrast to what happens during 2011 La Niña, as highlighted by Poulter *et al.* (*5*). During 2011, NBE anomalies were primarily driven by increased net carbon uptake in semiarid regions across the SH, with Australia itself accounting for 60% of net carbon flux anomalies (*17*, *37*). In contrast to the 2011 La Niña, only about 25% of the increased tropical net carbon uptake occurs over Australia in 2021 (Figs. 3 and 4). This difference could be attributed to lower precipitation and higher temperature over Australia in 2021 compared to 2011. Relative to 2011, the precipitation over Australia was 32% lower and temperature was 1.3°C higher (fig. S12).

Furthermore, in 2021, while the tropical GPP increase over semiarid regions and grassland/cropland is much larger than that over forests, a substantial portion of the increased carbon accumulation resulting from photosynthesis is released back to the atmosphere through increased respiration, likely due to an increased carbon pool from increased GPP and favorable climate conditions.

The determination of whether forests or semiarid regions serve as the primary drivers of net carbon flux interannual variability holds crucial implications for carbon-climate projections (*16*). This is because studies have shown that the response of carbon cycle to interannual climate variations are indicative of how carbon storage will respond to future climate change (*38*, *39*). Thus, whether tropical forests or semiarid regions have larger sensitivity to climate interannual variations would imply the vulnerability of their carbon storage to future climate change. The stark contrast of the response of tropical and SH land carbon cycle to the 2011 and 2021 La Niña events indicates that a long-term global CO_2 observation record that captures multiple ENSO cycles is essential to understand whether tropical forests or semiarid regions exert primary influence on the net carbon flux interannual variability and the vulnerability of their carbon storage to future climate change.

Implications

The close-to-normal atmospheric CO_2 growth rate in 2021 was the result of the compensation between increased net carbon uptake over the tropics and reduced net carbon uptake over the NH midlatitudes. Specifically, the extreme drought and warm anomalies over Europe and Asia reduced the net carbon uptake and offset 72% of the increased net carbon uptake over the tropics from the impact of the 2021 La Niña. By comparison, the atmospheric CO_2 growth rate was close to average in only two other La Niña events, 1975 and 1985 (Fig. 1). During those two events, the precipitation anomaly over central Asia (30°N to 50°N, 30°E to 85°E) was −15.6 and −16.7% during April to July in 1975 and 1985, respectively, while the precipitation anomaly was −22.6% in 2021 (figs. S19 and S20). In 1985, the precipitation reduction was more than 50% over part of the central Asia, comparable to the precipitation anomaly in 2021 (fig. S18). We speculate that the close-to-normal CO_2 growth rate in these 2 years may also have been caused by the opposite net carbon flux anomalies between the tropics and extra-tropics.

The frequency of extreme La Niña events is projected to become more frequent in the future (*40*). At the same time, CMIP6 models predict that the annual and early summer precipitation over central Asia is positively correlated with the ONI, suggesting reductions of precipitation over Central Asia during extreme La Niña years (fig. S21). Furthermore, positive vapor pressure deficit anomalies, especially during early summer, are projected by CMIP6 models during La Niña years. With the simultaneously increase of global temperature and predicted drying trend in western United States (IPCC AR6), our results imply that the regional compensation of flux anomalies between tropics and extra-tropics may become more frequent in future extreme La Niña events. The pivotal question of whether the CO_2 AF during La Niña events will remain lower than the average AF holds substantial implications for the trajectory of atmospheric CO_2 levels in the future. This underscores the critical importance to continue monitoring the natural carbon cycle at regional scales to inform and support effective carbon-climate policies.

MATERIALS AND METHODS

Top-down atmospheric CO_2 flux inversions with OCO-2 V10 MIP extensioXn

In this study, the top-down fluxes were generated with eight inversion models that are a subset of the models participating in the v10 OCO-2 MIP described by Byrne *et al.* (*14*) plus GCASv2 model that were documented in (*15*, *16*). These inversions were extended to the end of 2021. They used a combination of four transport models, three types of inversion algorithms, and two sources of meteorology fields (table S1). All the inversions used the same fossil fuel emissions and assimilated the same set of OCO-2 V10 retrievals (table S2). Because the number of surface flask observations was drastically different in 2021 at the time of this study (May 2022) because of data latency, which may affect the interannual variability analysis, we used the inversion results that assimilated OCO-2 V10 land retrievals only for the entire period (January 2015 to December 2021) in the Results. The original fossil fuel emission has 1° x 1° resolution. The data between 2015 and 2019 was from the official ODIAC website (https://db.cger.nies.go.jp/dataset/ODIAC/DL_odiac2022.html), while the fossil fuel emissions for 2020 and 2021 is scaled ODIAC emission using the country totals published by Carbon Monitor (*41*). Both air-sea exchange and NBE were optimized in these models, but the prior assumptions for these fluxes could be different (table S1). Table S2 lists all the assimilated observations and their sources.

The spatial resolution of these eight models is different, but all the posterior fluxes from these inversions were regridded to 1° × 1° resolution before analysis. The global annual net carbon fluxes calculated as the sum of fossil fuel emissions and natural carbon fluxes over land and ocean are consistent with the NOAA annual CO_2 growth based on marine surface network (fig. S2). The NOAA annual CO_2 growth in parts per million was converted to gigaton carbon per year (GtC/year) using the conversion factor 2.124 GtC/ppm (*42*). We assumed 0.2 GtC/year uncertainty for the observed annual CO_2 growth (*17*).

We calculated the mean across the ensembles as the best estimate and the SD as the uncertainty. The uncertainties of top-down NBE estimation come from the uncertainties in atmospheric transport models, observations, assumed prior natural carbon fluxes, and fossil fuel emissions. Even though we only have eight ensemble members, these top-down inversion models used a variety of transport models, inversion methodologies, and prior natural carbon fluxes (table S1). Thus, using ensemble SDs as NBE uncertainty enables us to capture the uncertainties in these aspects. However, because all these models used the same set of observations and fossil fuel emissions, the uncertainties in these aspects are not fully captured in the ensemble spread. As discussed in the section "The impact of fossil fuel emission uncertainties on flux anomaly estimation over East Asia," the NBE anomalies analyzed in this study are more sensitive to changes of fossil fuel emissions, which are consistent among different fossil fuel mission products. The SD among the ensemble inversions can still capture the uncertainties in observations, because the inversions assumed uncertainties (around 1 to 3 ppm) in these observations (*14*) even though all inversion models used the same set of observations. Note that the uncertainties estimated as the ensemble spread is different from uncertainties from individual models, which only include uncertainties in observations and prior fluxes and can significantly differ among each individual model (*14*).

We evaluated the posterior atmospheric CO_2 concentrations against observed CO_2 vertical profiles from ACT-America (*43*–*46*) campaign and CONTRAIL (*47*) included in (*46*) (figs. S4 to S7), because previous research suggests that the partition of carbon fluxes over the tropics and extra-tropics is sensitive to errors in CO_2 vertical gradient. As we focus on the flux anomalies, the results are not sensitive to the absolute errors in CO_2 vertical gradient but are sensitive to time-varying errors. We chose measurements from these two aircraft measurements because of their consistent observation coverage. CONTRAIL has observations over all the months over 2015–2017 and ACT-America has observations between 2016 and 2019. Because of data latency, there is no CONTRAIL in situ profiles publicly available for 2019–2021 at the time of this study and ACT-America field campaigns ended in 2019. The flask observations collected by the National Institute for Space Research over tropical South America might have higher measurement errors due to water vapor contamination, so we did not include those observations in the comparison. Despite the errors in vertical CO_2 gradient in each region, the errors are relatively constant from year to year, which indicates that the contrast of flux anomalies between tropics and extra-tropics are robust.

GPP estimates

We used two GPP products in this study: FluxSAT and GOSIF (*18*, *19*) (table S2). Both datasets were generated with machine learning approaches. FluxSAT was derived with neural networks that upscaled GPP from selected FLUXNET 2015 eddy covariance tower sites to a gridded global GPP with the input of Nadir Bidirectional Reflectance Distribution Function–Adjusted Reflectances (product from the MODIS instruments on the NASA Terra and Aqua satellites) (*48*). The FluxSAT provides global gridded daily estimates of GPP and uncertainties at 0.05-degree resolution.

GOSIF GPP was generated with the global, OCO-2 based SIF product (GOSIF) and linear relationship between SIF and GPP to map GPP globally at 0.05-degree resolution (*49*). GOSIF GPP product accounts for uncertainties of GPP estimates using eight SIF-GPP relationships with different forms. The GOSIF SIF product was generated with a machine learning approach that upscales OCO-2 SIF to a global product at 0.05-degree resolution with data from MODIS and meteorological reanalysis.

We regridded both products to 1° × 1° resolution and used the mean as the best estimate. We estimate uncertainties with a bootstrapping approach by randomly generating 1000 samples based on the difference between these two products.

Fire and TER

The monthly fire CO_2 emissions were documented (*50*) and estimated with a top-down atmospheric inversion assimilating CO observations from Measurements of Pollution in the Troposphere. The study in (*49*) does not include uncertainties, and we assumed a 20% uncertainty in the fire CO_2 emission anomalies. The TER was calculated as follows

$$\mathrm{TER} = \mathrm{NBE} + \mathrm{GPP} - \mathrm{FIRE}$$

The uncertainties for TER were calculated as

$$R_{\mathrm{TER}}^2 = R_{\mathrm{NBE}}^2 + R_{\mathrm{GPP}}^2 + R_{\mathrm{FIRE}}^2$$

where R_{TER}, R_{NBE}, R_{GPP}, R_{FIRE} are uncertainties for TER, NBE, GPP, and fire, respectively. Any fire-related land use land cover change (LULCC) anomalies were included in fire emissions, which is the largest component in the interannual variability of LULCC (*50*). Nonfire–related LULCC anomalies were included in other carbon flux components.

Because TER was calculated as the residual among NBE, GPP, and FIRE, we indirectly validated TER by validating NBE, GPP, and fire emissions. The GPP products have been validated against FLUXNET observations (*48*, *49*). We validated NBE through comparison against aircraft observations. The fire emission data was used by Zheng *et al.* (*26*).

Supplementary Materials

This PDF file includes:

Figs. S1 to S21
Tables S1 and S2
References

REFERENCES AND NOTES

1. P. Friedlingstein, M. W. Jones, M. O'Sullivan, R. M. Andrew, D. C. E. Bakker, J. Hauck, C. le Quéré, G. P. Peters, W. Peters, J. Pongratz, S. Sitch, J. G. Canadell, P. Ciais, R. B. Jackson, S. R. Alin, P. Anthoni, N. R. Bates, M. Becker, N. Bellouin, L. Bopp, T. T. T. Chau, F. Chevallier, L. P. Chini, M. Cronin, K. I. Currie, B. Decharme, L. M. Djeutchouang, X. Dou, W. Evans, R. A. Feely, L. Feng, T. Gasser, D. Gilfillan, T. Gkritzalis, G. Grassi, L. Gregor, N. Gruber, Ö. Gürses, I. Harris, R. A. Houghton, G. C. Hurtt, Y. Iida, T. Ilyina, I. T. Luijkx, A. Jain, S. D. Jones, E. Kato, D. Kennedy, K. Klein Goldewijk, J. Knauer, J. I. Korsbakken, A. Körtzinger, P. Landschützer, S. K. Lauvset, N. Lefèvre, S. Lienert, J. Liu, G. Marland,

P. C. McGuire, J. R. Melton, D. R. Munro, J. E. M. S. Nabel, S. I. Nakaoka, Y. Niwa, T. Ono, D. Pierrot, B. Poulter, G. Rehder, L. Resplandy, E. Robertson, C. Rödenbeck, T. M. Rosan, J. Schwinger, C. Schwingshackl, R. Séférian, A. J. Sutton, C. Sweeney, T. Tanhua, P. P. Tans, H. Tian, B. Tilbrook, F. Tubiello, G. R. van der Werf, N. Vuichard, C. Wada, R. Wanninkhof, A. J. Watson, D. Willis, A. J. Wiltshire, W. Yuan, C. Yue, X. Yue, S. Zaehle, J. Zeng, Global carbon budget 2021. *Earth Syst. Sci. Data* **14**, 1917–2005 (2022).

2. N. Zeng, A. Mariotti, P. Wetzel, Terrestrial mechanisms of interannual CO_2 variability. *Global Biogeochem. Cycles* **19**, GB1016 (2005).
3. P. J. Sellers, D. S. Schimel, B. Moore, J. Liu, A. Eldering, Observing carbon cycle–climate feedbacks from space. *Proc. Natl. Acad. Sci. U.S.A.* **115**, 7860–7868 (2018).
4. J. Worden, S. Saatchi, M. Keller, A. A. Bloom, J. Liu, N. Parazoo, J. B. Fisher, K. Bowman, J. T. Reager, K. Fahy, D. Schimel, R. Fu, S. Worden, Y. Yin, P. Gentine, A. G. Konings, G. R. Quetin, M. Williams, H. Worden, M. Shi, A. Barkhordarian, Satellite observations of the tropical terrestrial carbon balance and interactions with the water cycle during the 21st century. *Rev. Geophys.* **59**, e2020RG000711 (2021).
5. B. Poulter, D. Frank, P. Ciais, R. B. Myneni, N. Andela, J. Bi, G. Broquet, J. G. Canadell, F. Chevallier, Y. Y. Liu, S. W. Running, S. Sitch, G. R. van der Werf, Contribution of semi-arid ecosystems to interannual variability of the global carbon cycle. *Nature* **509**, 600–603 (2014).
6. O. L. Phillips, L. E. O. C. Aragão, S. L. Lewis, J. B. Fisher, J. Lloyd, G. López-González, Y. Malhi, A. Monteagudo, J. Peacock, C. A. Quesada, G. van der Heijden, S. Almeida, I. Amaral, L. Arroyo, G. Aymard, T. R. Baker, O. Bánki, L. Blanc, D. Bonal, P. Brando, J. Chave, A. C. OAlves de Oliveira, N. D. Cardozo, C. I. Czimczik, T. R. Feldpausch, M. A. Freitas, E. Gloor, N. Higuchi, E. Jiménez, G. Lloyd, P. Meir, C. Mendoza, A. Morel, D. A. Neill, D. Nepstad, S. Patiño, M. C. Peñuela, A. Prieto, F. Ramírez, M. Schwarz, J. Silva, M. Silveira, A. S. Thomas, H. T. Steege, J. Stropp, R. Vásquez, P. Zelazowski, E. A. Dávila, S. Andelman, A. Andrade, K.-J. Chao, T. Erwin, A. Di Fiore, E. Honorio, H. Keeling, T. J. Killeen, W. F. Laurance, A. P. Cruz, N. C. A. Pitman, P. N. Vargas, H. Ramírez-Angulo, A. Rudas, R. Salamão, N. Silva, J. Terborgh, A. Torres-Lezama, Drought sensitivity of the amazon rainforest. *Science* **323**, 1344–1347 (2009).
7. S. L. Lewis, P. M. Brando, O. L. Phillips, G. M. F. van der Heijden, D. Nepstad, The 2010 amazon drought. *Science* **331**, 554 (2011).
8. J. C. Jiménez-Muñoz, C. Mattar, J. Barichivich, A. Santamaría-Artigas, K. Takahashi, Y. Malhi, J. A. Sobrino, G. van der Schrier, Record-breaking warming and extreme drought in the Amazon rainforest during the course of El Niño 2015–2016. *Sci. Rep.* **6**, 33130 (2016).
9. K. W. Bowman, J. Liu, A. A. Bloom, N. C. Parazoo, M. Lee, Z. Jiang, D. Menemenlis, M. M. Gierach, G. J. Collatz, K. R. Gurney, D. Wunch, Global and brazilian carbon response to El Niño Modoki 2011–2010. *Earth Sp. Sci.* **4**, 637–660 (2017).
10. J. Wang, N. Zeng, M. Wang, F. Jiang, F. Chevallier, S. Crowell, W. He, M. S. Johnson, J. Liu, Z. Liu, S. M. Miller, S. Philip, H. Wang, M. Wu, W. Ju, S. Feng, M. Jia, Anomalous net biome exchange over amazonian rainforests induced by the 2015/16 El Niño: Soil dryness-shaped spatial pattern but temperature-dominated total flux. *Geophys. Res. Lett.* **50**, e2023GL103379 (2023).
11. J. Liu, K. W. Bowman, D. S. Schimel, N. C. Parazoo, Z. Jiang, M. Lee, A. A. Bloom, D. Wunch, C. Frankenberg, Y. Sun, C. W. O'dell, K. R. Gurney, D. Menemenlis, M. Gierach, D. Crisp, A. Eldering, Contrasting carbon cycle responses of the tropical continents to the 2015–2016 El Niño. *Science* **358**, eaam5690 (2017).
12. B. Byrne, J. Liu, M. Lee, Y. Yin, K. W. Bowman, K. Miyazaki, A. J. Norton, J. Joiner, D. F. Pollard, D. W. T. Griffith, V. A. Velazco, N. M. Deutscher, N. B. Jones, C. Paton-Walsh, The carbon cycle of southeast australia during 2019–2020: Drought, fires, and subsequent recovery. *AGU Adv.* **2**, e2021AV000469 (2021).
13. H. Peiro, S. Crowell, A. Schuh, D. Baker, C. O'Dell, A. Jacobson, F. Chevallier, J. Liu, A. Eldering, D. Crisp, F. Deng, B. Weir, S. Basu, M. S. Johnson, S. Philip, I. Baker, Four years of global carbon cycle observed from OCO-2 version 9 and in situ data, and comparison to OCO-2 v7. *Atmos. Chem. Phys.* **2021**, 1–50 (2021).
14. B. Byrne, D. F. Baker, S. Basu, M. Bertolacci, K. W. Bowman, D. Carroll, A. Chatterjee, F. Chevallier, P. Ciais, N. Cressie, D. Crisp, S. Crowell, F. Deng, Z. Deng, N. M. Deutscher, M. K. Dubey, S. Feng, O. E. García, D. W. T. Griffith, B. Herkommer, L. Hu, A. R. Jacobson, R. Janardanan, S. Jeong, M. S. Johnson, D. B. A. Jones, R. Kivi, J. Liu, Z. Liu, S. Maksyutov, J. B. Miller, S. M. Miller, I. Morino, J. Notholt, T. Oda, C. W. O'Dell, Y. S. Oh, H. Ohyama, P. K. Patra, H. Peiro, C. Petri, S. Philip, D. F. Pollard, B. Poulter, M. Remaud, A. Schuh, M. K. Sha, K. Shiomi, K. Strong, C. Sweeney, Y. Té, H. Tian, V. A. Velazco, M. Vrekoussis, T. Warneke, J. R. Worden, D. Wunch, Y. Yao, J. Yun, A. Zammit-Mangion, N. Zeng, National CO2 budgets (2015--2020) inferred from atmospheric CO2 observations in support of the global stocktake. *Earth Syst. Sci. Data* **15**, 963–1004 (2023).
15. F. Jiang, H. Wang, J. M. Chen, W. Ju, X. Tian, S. Feng, G. Li, Z. Chen, S. Zhang, X. Lu, J. Liu, H. Wang, J. Wang, W. He, M. Wu, Regional CO_2 fluxes from 2010 to 2015 inferred from GOSAT XCO_2 retrievals using a new version of the global carbon assimilation system. *Atmos. Chem. Phys.* **21**, 1963–1985 (2021).
16. W. He, F. Jiang, W. Ju, B. Byrne, J. Xiao, N. T. Nguyen, M. Wu, S. Wang, J. Wang, C. Rödenbeck, X. Li, M. Scholze, G. Monteil, H. Wang, Y. Zhou, Q. He, J. M. Chen, Do State-Of-The-Art Atmospheric CO_2 Inverse Models Capture Drought Impacts on the European Land Carbon Uptake? *J. Adv. Model. Earth Syst.* **15**, e2022MS003150 (2023).
17. P. Friedlingstein, M. O'Sullivan, M. W. Jones, R. M. Andrew, L. Gregor, J. Hauck, C. le Quéré, I. T. Luijkx, A. Olsen, G. P. Peters, W. Peters, J. Pongratz, C. Schwingshackl, S. Sitch, J. G. Canadell, P. Ciais, R. B. Jackson, S. R. Alin, R. Alkama, A. Arneth, V. K. Arora, N. R. Bates, M. Becker, N. Bellouin, H. C. Bittig, L. Bopp, F. Chevallier, L. P. Chini, M. Cronin, W. Evans, S. Falk, R. A. Feely, T. Gasser, M. Gehlen, T. Gkritzalis, L. Gloege, G. Grassi, N. Gruber, Ö. Gürses, I. Harris, M. Hefner, R. A. Houghton, G. C. Hurtt, Y. Iida, T. Ilyina, A. K. Jain, A. Jersild, K. Kadono, E. Kato, D. Kennedy, K. Klein Goldewijk, J. Knauer, J. I. Korsbakken, P. Landschützer, N. Lefèvre, K. Lindsay, J. Liu, Z. Liu, G. Marland, N. Mayot, M. J. McGrath, N. Metzl, N. M. Monacci, D. R. Munro, S. I. Nakaoka, Y. Niwa, K. O'Brien, T. Ono, P. I. Palmer, N. Pan, D. Pierrot, K. Pocock, B. Poulter, L. Resplandy, E. Robertson, C. Rödenbeck, C. Rodriguez, T. M. Rosan, J. Schwinger, R. Séférian, J. D. Shutler, I. Skjelvan, T. Steinhoff, Q. Sun, A. J. Sutton, C. Sweeney, S. Takao, T. Tanhua, P. P. Tans, X. Tian, H. Tian, B. Tilbrook, H. Tsujino, F. Tubiello, G. R. van der Werf, A. P. Walker, R. Wanninkhof, C. Whitehead, A. Willstrand Wranne, R. Wright, W. Yuan, C. Yue, X. Yue, S. Zaehle, J. Zeng, B. Zheng, Global Carbon Budget 2022. *Earth Syst. Sci. Data* **14**, 4811–4900 (2022).
18. C. Rödenbeck, S. Houweling, M. Gloor, M. Heimann, CO_2 flux history 1982–2001 inferred from atmospheric data using a global inversion of atmospheric transport. *Atmos. Chem. Phys.* **3**, 1919–1964 (2003).
19. P. Bousquet, P. Peylin, P. Ciais, C. Le Quéré, P. Friedlingstein, P. P. Tans, Regional Changes in Carbon Dioxide Fluxes of Land and Oceans Since 1980. *Science* **290**, 1342–1347 (2000).
20. D. F. Baker, R. M. Law, K. R. Gurney, P. Rayner, P. Peylin, A. S. Denning, P. Bousquet, L. Bruhwiler, Y. H. Chen, P. Ciais, I. Y. Fung, M. Heimann, J. John, T. Maki, S. Maksyutov, K. Masarie, M. Prather, B. Pak, S. Taguchi, Z. Zhu, TransCom 3 inversion intercomparison: Impact of transport model errors on the interannual variability of regional CO2 fluxes, 1988–2003. *Global Biogeochem. Cycles* **20**, 10.1029/2004GB002439 (2006).
21. R. J. Leamon, The triple-dip La Niña of 2020–22: Updates to the correlation of ENSO with the termination of solar cycles. *Front. Earth Sci.* **11**, 10.3389/feart.2023.1204191 (2023).
22. C. Gao, M. Chen, L. Zhou, L. Feng, R. H. Zhang, The 2020–2021 prolonged La Niña evolution in the tropical Pacific. *Sci. China Earth Sci.* **65**, 2248–2266 (2022).
23. B. Gaubert, B. B. Stephens, S. Basu, F. Chevallier, F. Deng, E. A. Kort, P. K. Patra, W. Peters, C. Rödenbeck, T. Saeki, D. Schimel, I. Van der Laan-Luijkx, S. Wofsy, Y. Yin, Global atmospheric CO_2 inverse models converging on neutral tropical land exchange but diverging on fossil fuel and atmospheric growth rate. *Biogeosciences* **16**, 117–134 (2018).
24. B. B. Stephens, K. R. Gurney, P. P. Tans, C. Sweeney, W. Peters, L. Bruhwiler, P. Ciais, M. Ramonet, P. Bousquet, T. Nakazawa, S. Aoki, T. Machida, G. Inoue, N. Vinnichenko, J. Lloyd, A. Jordan, M. Heimann, O. Shibistova, R. L. Langenfelds, L. Paul Steele, R. J. Francey, A. S. Denning, Weak northern and strong tropical land carbon uptake from vertical profiles of atmospheric CO_2. *Science* **316**, 1732–1735 (2007).
25. A. E. Schuh, A. R. Jacobson, Uncertainty in parameterized convection remains a key obstacle for estimating surface fluxes of carbon dioxide. *Atmos. Chem. Phys.* **23**, 6285–6297 (2023).
26. B. Zheng, P. Ciais, F. Chevallier, H. Yang, J. G. Canadell, Y. Chen, I. R. van der Velde, I. Aben, E. Chuvieco, S. J. Davis, M. Deeter, C. Hong, Y. Kong, H. Li, H. Li, X. Lin, K. He, Q. Zhang, Record-high CO_2 emissions from boreal fires in 2021. *Science* **379**, 912–917 (2023).
27. A. A. Bloom, J.-F. Exbrayat, I. R. van der Velde, L. Feng, M. Williams, The decadal state of the terrestrial carbon cycle: Global retrievals of terrestrial carbon allocation, pools, and residence times. *Proc. Natl. Acad. Sci. U.S.A.* **113**, 1285–1290 (2016).
28. N. Madani, J. S. Kimball, N. C. Parazoo, A. P. Ballantyne, T. Tagesson, L. A. Jones, R. H. Reichle, P. I. Palmer, I. Velicogna, A. A. Bloom, S. Saatchi, Z. Liu, A. Geruo, Below-surface water mediates the response of African forests to reduced rainfall. *Environ. Res. Lett.* **15**, 34063 (2020).
29. B. D. Stocker, S. J. Tumber-Dávila, A. G. Konings, M. C. Anderson, C. Hain, R. B. Jackson, Global patterns of water storage in the rooting zones of vegetation. *Nat. Geosci.* **16**, 250–256 (2023).
30. Y. Fan, G. Miguez-Macho, E. G. Jobbágy, R. B. Jackson, C. Otero-Casal, Hydrologic regulation of plant rooting depth. *Proc. Natl. Acad. Sci. U.S.A.* **114**, 10572 (2017).
31. T. Zhou, W. Zhang, L. Zhang, R. Clark, C. Qian, Q. Zhang, H. Qiu, J. Jiang, X. Zhang, 2021: A year of unprecedented climate extremes in Eastern Asia, North America, and Europe. *Adv. Atmos. Sci.* **39**, 1598–1607 (2022).
32. A. Bastos, I. A. Janssens, C. M. Gouveia, R. M. Trigo, P. Ciais, F. Chevallier, J. Peñuelas, C. Rödenbeck, S. Piao, P. Friedlingstein, S. W. Running, European land CO_2 sink influenced by NAO and East-Atlantic Pattern coupling. *Nat. Commun.* **7**, 10315 (2016).
33. J. Wang, M. Wang, J. S. Kim, J. Joiner, N. Zeng, F. Jiang, H. Wang, W. He, M. Wu, T. Chen, W. Ju, J. M. Chen, Modulation of land photosynthesis by the indian ocean dipole: Satellite-based observations and CMIP6 future projections. *Earth's Future* **9**, e2020EF001942 (2021).
34. J.-S. Kim, J.-S. Kug, S.-J. Jeong, H. Park, G. Schaepman-Strub, Extensive fires in southeastern Siberian permafrost linked to preceding Arctic Oscillation. *Sci. Adv.* **6**, eaax3308 (2020).

35. R. J. Andres, T. A. Boden, D. M. Higdon, Gridded uncertainty in fossil fuel carbon dioxide emission maps, a CDIAC example. *Atmos. Chem. Phys.* **16**, 14979–14995 (2016).
36. A. P. Ballantyne, R. Andres, R. Houghton, B. D. Stocker, R. Wanninkhof, W. Anderegg, L. A. Cooper, M. DeGrandpre, P. P. Tans, J. B. Miller, C. Alden, J. W. C. White, Audit of the global carbon budget: Estimate errors and their impact on uptake uncertainty. *Biogeosciences* **12**, 2565–2584 (2015).
37. M. G. Bosilovich, F. R. Robertson, P. W. Stackhouse, El Niño–Related Tropical Land Surface Water and Energy Response in MERRA-2. *J. Climate* **33**, 1155–1176 (2020).
38. P. M. Cox, D. Pearson, B. B. Booth, P. Friedlingstein, C. Huntingford, C. D. Jones, C. M. Luke, Sensitivity of tropical carbon to climate change constrained by carbon dioxide variability. *Nature* **494**, 341–344 (2013).
39. A. Barkhordarian, K. W. Bowman, N. Cressie, J. Jewell, J. Liu, Emergent constraints on tropical atmospheric aridity–carbon feedbacks and the future of carbon sequestration. *Environ. Res. Lett.* **16**, 114008 (2021).
40. W. Cai, G. Wang, A. Santoso, M. J. McPhaden, L. Wu, F. F. Jin, A. Timmermann, M. Collins, G. Vecchi, M. Lengaigne, M. H. England, D. Dommenget, K. Takahashi, E. Guilyardi, Increased frequency of extreme La Niña events under greenhouse warming. *Nat. Clim. Chang.* **5**, 132–137 (2015).
41. S. Basu, R. Nassar, *Fossil Fuel* CO_2 *Emissions for the OCO2 Model Intercomparison Project (MIP)*. 10.5281/zenodo.8325420 (2023).
42. C. L. Quéré, R. M. Andrew, P. Friedlingstein, S. Sitch, J. Pongratz, A. C. Manning, J. I. Korsbakken, G. P. Peters, J. G. Canadell, R. B. Jackson, T. A. Boden, P. P. Tans, O. D. Andrews, V. K. Arora, D. C. E. Bakker, L. Barbero, M. Becker, R. A. Betts, L. Bopp, F. Chevallier, L. P. Chini, P. Ciais, C. E. Cosca, J. Cross, K. Currie, T. Gasser, I. Harris, J. Hauck, V. Haverd, R. A. Houghton, C. W. Hunt, G. Hurtt, T. Ilyina, A. K. Jain, E. Kato, M. Kautz, R. F. Keeling, K. K. Goldewijk, A. Körtzinger, P. Landschützer, N. Lefèvre, A. Lenton, S. Lienert, I. Lima, D. Lombardozzi, N. Metzl, F. Millero, P. M. S. Monteiro, D. R. Munro, J. E. M. S. Nabel, S.-I. Nakaoka, Y. Nojiri, X. A. Padin, A. Peregon, B. Pfeil, D. Pierrot, B. Poulter, G. Rehder, J. Reimer, C. Rödenbeck, J. Schwinger, R. Séférian, I. Skjelvan, B. D. Stocker, H. Tian, B. Tilbrook, F. N. Tubiello, I. T. van der Laan-Luijkx, G. R. van der Werf, S. van Heuven, N. Viovy, N. Vuichard, A. P. Walker, A. J. Watson, A. J. Wiltshire, S. Zaehle, D. Zhu, Global Carbon Budget 2017. *Earth Syst. Sci. Data* **10**, 405–448 (2018).
43. K. J. Davis, M. D. Obland, B. Lin, T. Lauvaux, C. O'Dell, B. Meadows, E. V. Browell, J. P. DiGangi, C. Sweeney, M. J. McGill, J. D. Barrick, A. R. Nehrir, M. M. Yang, J. R. Bennett, B. C. Baier, A. Roiger, S. Pal, T. Gerken, A. Fried, S. Feng, R. Shrestha, M. A. Shook, G. Chen, L. J. Campbell, Z. R. Barkley, R. M. Pauly, *ACT-America: L3 Merged In Situ Atmospheric Trace Gases and Flask Data, Eastern USA*. 10.3334/ORNLDAAC/1593 (2018).
44. Y. Wei, R. Shrestha, S. Pal, T. Gerken, S. Feng, J. McNelis, D. Singh, M. M. Thornton, A. G. Boyer, M. A. Shook, G. Chen, B. C. Baier, Z. R. Barkley, J. D. Barrick, J. R. Bennett, E. V. Browell, J. F. Campbell, L. J. Campbell, Y. Choi, J. Collins, J. Dobler, M. Eckl, A. Fiehn, A. Fried, J. P. Digangi, R. Barton-Grimley, H. Halliday, T. Klausner, S. Kooi, J. Kostinek, T. Lauvaux, B. Lin, M. J. McGill, B. Meadows, N. L. Miles, A. R. Nehrir, J. B. Nowak, M. Obland, C. O'Dell, R. M. P. Fao, S. J. Richardson, D. Richter, A. Roiger, C. Sweeney, J. Walega, P. Weibring, C. A. Williams, M. M. Yang, Y. Zhou, K. J. Davis, Atmospheric Carbon and Transport–America (ACT-America) Data Sets: Description, Management, and Delivery. *Earth Space Sci.* **8**, e2020EA001634 (2021).
45. K. J. Davis, E. V. Browell, S. Feng, T. Lauvaux, M. D. Obland, S. Pal, B. C. Baier, D. F. Baker, I. T. Baker, Z. R. Barkley, K. W. Bowman, Y. Y. Cui, A. S. Denning, J. P. DiGangi, J. T. Dobler, A. Fried, T. Gerken, K. Keller, B. Lin, A. R. Nehrir, C. P. Normile, C. W. O'Dell, L. E. Ott, A. Roiger, A. E. Schuh, C. Sweeney, Y. Wei, B. Weir, M. Xue, C. A. Williams, The Atmospheric Carbon and Transport (ACT)-America Mission. *Bull. Am. Meteorol. Soc.* **102**, E1714–E1734 (2021).
46. B. C. Baier, C. Sweeney, Y. Choi, K. J. Davis, J. P. DiGangi, S. Feng, A. Fried, H. Halliday, J. Higgs, T. Lauvaux, B. R. Miller, S. A. Montzka, T. Newberger, J. B. Nowak, P. Patra, D. Richter, J. Walega, P. Weibring, Multispecies assessment of factors influencing regional CO_2 and CH_4 enhancements during the winter 2017 ACT-America campaign. *J. Geophys. Res. Atmos.* **125**, e2019JD031339 (2020).
47. T. Machida, H. Matsueda, Y. Sawa, Y. Nakagawa, K. Hirotani, N. Kondo, K. Goto, T. Nakazawa, K. Ishikawa, T. Ogawa, Worldwide measurements of atmospheric CO_2 and other trace gas species using commercial airlines. *J. Atmos. Oceanic Tech.* **25**, 1744–1754 (2008).
48. J. Joiner, Y. Yoshida, Agricultural and Forest Meteorology Satellite-based re fl ectances capture large fraction of variability in global gross primary production (GPP) at weekly time scales. *Agric. For. Meteorol.* **291**, 108092 (2020).
49. X. Li, J. Xiao, Mapping photosynthesis solely from solar-induced chlorophyll fluorescence: A global, fine-resolution dataset of gross primary production derived from OCO-2. *Remote Sens.* **11**, 2563 (2019).
50. B. Zheng, *Global fire CO2 emissions 2000–2021*. 10.6084/m9.figshare.21770624.v1 (2022).
51. L. Gu, D. D. Baldocchi, S. C. Wofsy, J. William Munger, J. J. Michalsky, S. P. Urbanski, T. A. Boden, Response of a deciduous forest to the mount pinatubo eruption: Enhanced photosynthesis. *Science* **299**, 2035–2038 (2003).
52. V. Eyring, S. Bony, G. A. Meehl, C. A. Senior, B. Stevens, R. J. Stouffer, K. E. Taylor, Overview of the coupled model intercomparison project phase 6 (CMIP6) experimental design and organization. *Geosci. Model Dev.* **9**, 1937–1958 (2016).

Acknowledgments

Funding: Part of the research was carried out at the Jet Propulsion Laboratory, California Institute of Technology, under a contract with NASA (80NM0018D0004). J.X. was supported by the National Science Foundation (NSF) (Macrosystem Biology & NEON-Enabled Science program: DEB-2017870). S.M.M. acknowledges the NASA funding support 80NSSC21K1073. F.C. would like to acknowledge the funding support from Copernicus Atmosphere Monitoring Service, implemented by ECMWF on behalf of the European Commission (grant: CAMS2 55 bis), and the HPC resources of TGCC under the allocation A0130102201 made by GENCI. M.S.J. acknowledges the internal funding from NASA's Earth Science Research and Analysis Program. **Author contributions:** Conceptualization: J.L. Methodology: J.L., D.B., S.B., K.B., B.B., F.C., W.H., F.J., M.S.J., T.L.K., X.L., Z.L., S.M.M., S.P., J.X., and N.Z. Investigation: J.L., D.B., S.B., K.B., B.B., F.C., W.H., F.J., M.S.J., X.L., Z.L., S.M.M., S.P., J.X., and N.Z. Visualization: J.L. and J.Y. Writing—original draft: J.L. Writing—review and editing: All coauthors contributed to reviewing and editing. **Competing interests:** The authors declare they have no competing interests. **Data and materials availability:** All data needed to evaluate the conclusions in the paper are present in the paper and/or the Supplementary Materials. All the data sources are listed in table S2 and publicly available.

Submitted 5 October 2023
Accepted 2 May 2024
Published 7 June 2024
10.1126/sciadv.adl2201